

Influence of structural characteristics on magnetic properties in face-centered-tetragonal surface alloy of Fe/Pd(100) ultrathin films

C. Boeglin, H. Bulou, J. Hommet, and X. Le Cann*

Institut de Physique et Chimie des Matériaux de Strasbourg, Groupe Surfaces Interfaces, UMR 7504, 23, rue du Loess, Boîte Postale 20CR, F-67037 Strasbourg, France

H. Magnan

*Commissariat à l'Énergie Atomique, DRECAM-SRSIM, 91191 Gif-sur-Yvette, France
and LURE, UMR 130, Université de Paris-Sud, 91405 Orsay, France*

P. Le Fèvre and D. Chandèsris

LURE, UMR 130, Université de Paris-Sud, 91405 Orsay, France

(Received 28 December 1998; revised manuscript received 30 March 1999)

Ultrathin Fe layers grown at room temperature (RT) on Pd(100) show anomalous magnetic in-plane anisotropy even in the monolayer limit whereas perpendicular anisotropy can be achieved only by depositing iron layers at lower temperature. The structure of the RT grown films and its influence on the magnetic properties are examined. In order to clarify the growth at RT, we have performed core level photoemission, LEED and SEXAFS on ultrathin Fe/Pd(100) layers. By photoemission, we observe a core level shift which is attributed to the interdiffusion of the first iron layers into the Pd(100) substrate. SEXAFS measurements confirm a surface alloying up to four equivalent monolayers Fe/Pd(100). At this coverage, polarization dependent SEXAFS results are compatible with a face-centered-tetragonal Fe₅₅/Pd₄₅ disordered alloy structure showing an expansion of 4% of the lattice parameter in the growth direction. The magnetic in plane anisotropy observed by Kerr on ultrathin Fe films and the large orbital moment measured on the Fe L_{2,3} edges are understood in the light of the microscopic description of the Fe/Pd(100) interface. [S0163-1829(99)01830-5]

I. INTRODUCTION

Many experimental and theoretical results have been obtained in the past fifteen years in the field of magnetic multilayers. In these artificially grown low-dimensional magnetic systems the interfaces are of greatest importance and often play a key role. The macroscopic magnetic properties of these systems are widely related to their structure on the microscopic scale. It was shown in the eighties that the Cd/Au and Co/Pd multilayers exhibit in-plane anisotropy induced respectively by rough interfaces and interfacial mixing.^{1,2} Detailed growth studies of the related single ultrathin films give access to the interface and film structure and can thus be considered as model systems for the understanding of the multilayered systems.

Dimensionality effects (form anisotropy) in these systems lead to the well-known perpendicular anisotropy observed in the Cd/Cu(100), Ni/Cu(100), Fe/Cu(100), Fe/Cu(111) (Refs. 3–7) thin films. On the other hand, the coupling at the interfaces (through *d* band hybridization) was thought to be at the origin of the strong magnetic anisotropy observed in Co/Au(111), Co/Pt(111), or Co/Pd(111).^{8–12} For thin films and multilayers, the combination of 3*d*-4*d* or 3*d*-5*d* transition metals takes advantage of the *d* band hybridization at the interface and of the exchange interactions. Magnetoelastic effects introduced by elastic deformation of unit cells of the epitaxial layers and magnetocrystalline effects due to the structure are also important contributions to the macroscopic magnetic anisotropy.^{13–18} In itinerant ferromagnetic materials, the recently developed x-ray magnetic circular dichroism

(XMCD) (more recently in the transverse geometry) leads to a direct measurement of spin and orbital anisotropy.^{19,20} These are the main ideas behind the theory in the field of orbital magnetism and its connection to magnetocrystalline anisotropy.²¹

The question which is addressed in this work is that of the microscopic origin of the strong magnetic in-plane anisotropy in Fe/Pd(100) ultrathin films. It is known that the lattice mismatch between bcc Fe and fcc Pd favors a strong tetragonalization of the epitaxial iron layers.^{22,23} Since the strain would induce a magnetoelastic surface anisotropy and thus favor perpendicular magnetic anisotropy (PMA) it cannot be at the origin of the observed in-plane anisotropy.

In this paper, the SEXAFS analysis will be used to show that the ultrathin films are face-centered-tetragonal (fct) surface alloy close to the well known disordered γ phase of Fe₅₀Pd₅₀. This surface alloy shows a perpendicular tetragonalization and is thus different from the γ phase. At room temperature diffusion mechanisms at the Fe/Pd(100) ultrathin film interface and the strong magnetic in-plane anisotropy²⁴ can both be discussed within the presented microscopic model.

Only a few attempts were made to understand precisely the crystallographic structure and the morphology of the ultrathin iron films in the monolayer range.^{23,25,26} At low temperature the LEED pattern is diffuse whereas at room temperature the different spots become sufficiently sharp after 12 ML to be fully analyzed by *I(V)* methods.²⁷ The results show that the structure of the film is bct at 12 ML Fe/Pd(100) and relaxes to bcc only for very thick layers (100

ML). The distortion was attributed to a slow reduction of the epitaxial strain at the Fe/Pd(100) interface. The sharpness of the interface is still somewhat controversial. Various authors have tried to define the sharpness of the ultrathin film interfaces. However, their arguments were only partially supported by RHEED, Auger spectroscopy or magnetic properties.^{22,24–26,28}

Some authors have shown by magneto-optical Kerr effect measurements, polarized-neutron reflection, or magnetic x-ray circular dichroism that the easy axis is in-plane and along the [100] direction^{22,24,25,29} in the case of RT deposited ultrathin Fe/Pd(100) films. Since low temperature grown iron films show the expected PMA,^{25,26} there is a close relationship between the morphology of these films and their magnetic properties.

In this paper we will focus on the structure of the iron films and on the related in-plane magnetic anisotropy as well as on the values of the orbital magnetic moments measured at the $L_{2,3}$ Fe edges. In Sec. III, *in situ* magneto-optical Kerr effect measurements are presented for RT grown 1.7 ML to 5 ML films. The extracted anisotropy constant K_v is found to be larger by a factor 10 compared to Fe bcc. The constant will be discussed and compared to MBE coevaporated $\text{Fe}_{50}\text{Pd}_{50}/\text{MgO}(100)$.³⁰ The previously published magnetic circular dichroism data and the large orbital moment measured along the [100] in-plane direction which were still unexplained are compared to recent MCXD data obtained on MBE coevaporated $\text{Fe}_{50}\text{Pd}_{50}/\text{MgO}(100)$.^{24,31}

The structural description of the ultrathin Fe/Pd(100) films is presented in Sec. IV and is supported by an extensive core level photoemission analysis completed by LEED- $I(V)$ data and an SEXAFS study. The 3d Pd core level shift observed after iron deposition is directly related to the mean chemical environment of the topmost layers, whereas the EXAFS performed at the Fe K edge gives the short range order over the whole film. The linear polarization of the x-ray radiation allows us to get information about the anisotropy of the crystallographic structure through an independent measurement of the interatomic distances in and out of the film plane. Furthermore, EXAFS spectra recorded at the Fe K -edge are sensitive to interdiffusion at the interface since in our case the contributions of the Pd atoms can be separated from the Fe contributions in the EXAFS oscillations.

In Sec. V, we discuss and explain the magnetic data in the light of the structural characteristics of the RT grown Fe/Pd(100) films.

II. EXPERIMENTS

The magneto-optical Kerr effect measurements were performed on an *in situ* grown Fe/Pd(100) wedge from 0 to 7 ML Fe/Pd(100) and calibrated by Auger electron spectroscopy (AES). The laser spot size on the sample was less than 0.5 mm^2 in order to assume a single domain in the Kerr analysis.

The SEXAFS experiments were performed at the “Laboratoire pour l’Utilisation du Rayonnement Electromagnetique” (LURE) on the surface EXAFS setup using a Ge(220) double crystals monochromator installed on the wiggler beam line of the DCI storage ring. Photoemission data were recorded using monochromatized x rays of the $\text{AlK}\alpha$ line

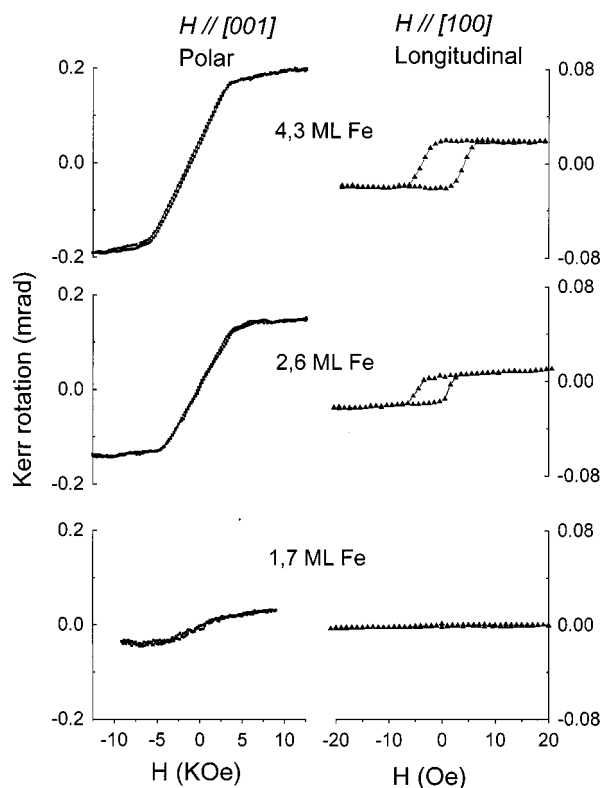


FIG. 1. Polar and longitudinal Kerr-effect rotation for Fe/Pd(100) grown at room temperature. The longitudinal Kerr-effect loop appears after 1.7 ML Fe/Pd(100). Polar Kerr-effect signal shows that the out of plane [001] direction is the hard axis between 1.5 ML Fe and 5 ML Fe/Pd(100).

and recorded with a high-resolution hemispherical energy analyzer in the normal emission direction. The Fe films were grown at room temperature in ultrahigh vacuum (base pressure 1×10^{-10} mbar). The film thickness was calibrated by a quartz crystal microbalance and controlled by AES. In both experiments the typical growth rate was 0.2 ML min^{-1} which insures that variations in the growth process due to surface kinetic effects are minimized. Further details of the sample preparation are given in Refs. 23 and 24. In the SEXAFS experiment the variation of the x-ray absorption coefficient of the samples was measured in the fluorescence yield mode above the K edge of iron (7114 eV). In order to get information about the crystallographic anisotropy the spectra were recorded in normal incidence with the linear polarization parallel to the surface (100) plane of the sample and in grazing incidence using an angle of incidence of 75° .

III. MAGNETIC PROPERTIES

The polar and the longitudinal magneto-optical Kerr rotation obtained on a Fe/Pd(100) wedge grown sample are shown in Fig. 1 for 1.7 ML up to 4.3 ML Fe/Pd(100). Along the [100] direction the onset of the hysteresis loop is observed at room temperature between 1.7 and 2 ML Fe/Pd(100) corresponding to the MCXD data.²⁴ The discrepancy with previous data²⁵ where it was found to occur at 1 ML is related to our Auger calibration (no exponential decay of the Pd line) which leads to a different monolayer definition.²³ In the polar Kerr geometry the magnetization is

clearly along the hard axis [001] where we observe for our thin films a linear evolution of the anisotropy field with the inverse of the equivalent thickness e of the iron film. The volume respectively interface anisotropy constants K_u respectively K_s are given by $K_u = 6.4 \times 10^6$ erg/cm³ and $K_s = -0.7 \times 10^{-2}$ erg/cm².

The extracted Kerr anisotropy constant K_v of 6.4×10^6 erg/cm³ is found to be larger of a factor 10 compared to Fe bcc (4.2×10^5 erg/cm³) but close to the set of MBE coevaporated Fe₅₀Pd₅₀/MgO(100) values ($K_u = (2-10) \times 10^6$ erg/cm³) obtained for different chemical ordering.^{30,31} The similarity of the anisotropy constants between our ultrathin films and the coevaporated 500 Å Fe₅₀Pd₅₀/MgO(100) is an indication for a surface alloy in the case of RT grown 3 ML Fe/Pd(100).

The magnetic orbital moment has been extensively studied by MCXD in a previous paper²⁴ where surprisingly large orbital moments were found ($0.54 \pm 0.07 \mu_B$) for RT deposited 2 ML up to 5 ML Fe/Pd(100) compared to bulk bcc Fe ($0.09 \mu_B$).³² For the same samples the out of plane MCXD signal was zero in the magnetic remanent state.

The previously published magnetic circular dichroism data and the large orbital moment measured along the [100] in-plane direction which were still unexplained can be compared to recent MCXD data obtained on MBE coevaporated Fe₅₀Pd₅₀/MgO(100).³¹ For the different elaboration temperature of the MBE alloys the orbital moment was found of ($0.22 \pm 0.05 \mu_B$) in the chemically disordered sample and up to ($0.42 \pm 0.05 \mu_B$) in the ordered one.

Ultrathin films Fe/Pd(100) grown at RT show in-plane anisotropy which is also the case in the disordered MBE alloys and we believe that an intermediate chemical order in our 3 ML Fe/Pd(100) film could explain the large orbital moment found by MCXD and the magnetic anisotropy analyzed by the magneto-optical Kerr measurements.

IV. STRUCTURE OF THE FILMS

In Fig. 2 we show the evolution of the Pd 3d core level after deposition of 6 ML Fe/Pd(100) at room temperature and different annealing of the film which favor interdiffusion monitored by Auger spectroscopy. The mean free path for the Pd 3d photoelectrons (1100 eV kinetic energy) is estimated to 15 Å. For this reason the surface related component is below the detection limit in the normal emission geometry, compared to the bulk Pd 3d contribution. We notice in Fig. 2 that the spectrum undergoes a strong broadening at 6 ML Fe/Pd(100). This evolution is progressive with film thickness and shows a saturation at about 4 ML. Considering the relatively large mean free path, the shifted photoelectron line obviously probe more than a single Fe/Pd interface layer.

We can notice that the experimental spectra of the 400 °C annealed 6 ML film show no contribution of bulk Pd 3d. This implies that the Fe concentration in the probed interface alloy is less than 50% by considering the mean free path of the photoelectrons (15 Å) combined with the initially amount of 6 ML Fe. The confirmation is given by the Pd 3d core level shift of 0.60 eV related to 38% iron concentration as extracted from the concentration versus binding energy equation (1):

$$\Delta E = 1.6C, \quad (1)$$

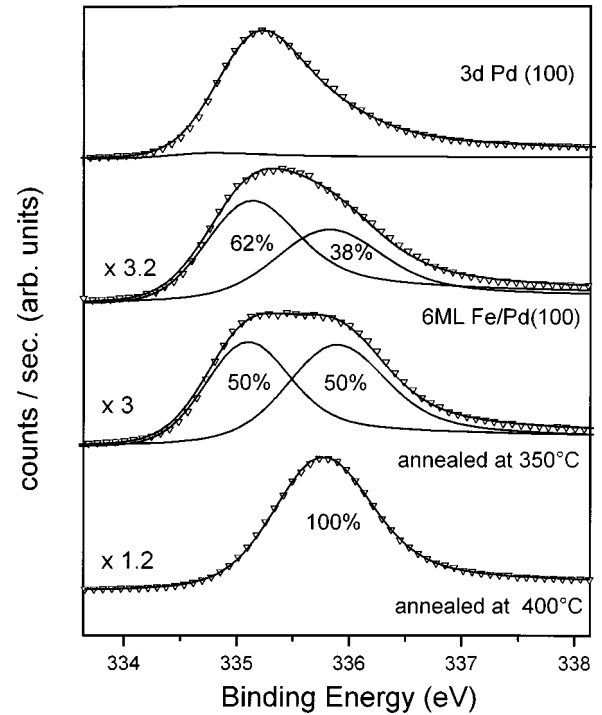


FIG. 2. Pd 3d core level photoemission spectra recorded with a monochromatized x-ray Al $K\alpha$ source, for clean Pd(100), 6 ML Fe/Pd(100) room temperature grown film and for the annealed films at 350 and 400 °C. The open triangles are the experimental data points and the continuous lines are the total intensity of the simulated photoemission lines obtained by the addition of two contributions: one for bulk Pd 3d and the other for FePd alloy Pd 3d.

where ΔE is the energy shift in eV and C the iron concentration. The estimation of the core level shift (related in this case to alloying of Pd) has been proposed by Johansson and Martensson.³³ The photoemission process is analyzed in terms of a Born-Haber cycle involving the cohesion energy, the ionization energy and the energy of solution calculated after Miedema *et al.*³⁴

The core level energy position of the alloy obtained by the 400 °C annealing is 0.60 eV with respect to the bulk Pd 3d. The Pd 3d core level energy position is thus coherent with a 38% Fe concentration. We suppose that the single core level lineshape of the alloy given by the 400 °C annealed film represents a good line shape reference for the alloy component in our thin films and that the energy position is related to the specific concentration.

Annealing a thicker film of 20 ML Fe/Pd(100) (not shown) at 400 °C leads to the same shape and position of the Pd 3d core level as observed for the annealed 6 ML Fe. Obviously the average concentration after the 400 °C annealing at the surface is equivalent in concentration whether we start with 6 ML or 20 ML Fe/Pd(100). This could be understood by a temperature dependent concentration in the surface alloy.

The bulk and alloy components were described by asymmetric line profiles including both Lorentzian and Gaussian functions and the parameters controlling the detailed line shape were optimized for a best fit to the experimental spectra of clean Pd(100) and 400 °C annealed film.

The decomposition performed on each photoemission spectra has been obtained by taking a combination of the

fitted shape obtained for the clean Pd(100) and for the 400 °C annealed 6 ML sample where a complete diffused situation is assumed.

The total Gaussian broadening in the fitted lines was 0.8 eV. The adjusted Lorentzian parameter was 0.13 and the asymmetry parameter 0.15 corresponding to the fit parameter found on Pd(100) by Andersen.³⁵ The energy position of the bulk component was fixed to the value found for the clean Pd(100) spectra at 334.95 eV after the Fermi energy correction. For the different situations the alloy corresponding lines have been adjusted for their energy position considering dilution effects of the iron into the Pd surface. The surface peak position has been fixed at 334.52 eV binding energy corresponding to previous work of Nyholm *et al.*³⁶ The contribution of this surface related line could be neglected in the experiment as shown in Fig. 2.

The RT grown 6 ML Fe/Pd(100) film can be simulated by a combination of the already described photoemission lines (bulk Pd 3*d* and Pd 3*d* alloy) and the best energy adjustment for the alloy contribution is obtained for a binding energy of 335.68 eV (+0.74 eV with respect to the bulk peak position). Following Eq. (1) the line at 335.68 eV corresponds to a 46% Fe average concentration in the local environment of Pd.

Considering the 6 ML situation we notice that the relative areas of the bulk component and alloy component are respectively 62% and 38%. Supposing a constant Fe concentration over the interface alloy (Fe₄₆Pd₅₄) the photoelectron mean free path of 15 Å implies that we have a 14 Å thick alloy at the interface in order to describe the two relative Pd 3*d* photoemission components. Considering the fct parameter of 3.90 Å given by the structural analysis (see next sections), a simple calculation shows that 3.8 equivalent Fe monolayers are imbedded in the Pd(100) surface and that about 2 ML Fe are on top of the interface alloy.

As it can be observed, the relative bulk to alloy components (50%,50%) for the 350 °C annealed film shows that more Pd atoms are involved in the alloy of the above defined concentration as for the room temperature grown film. After annealing at 350 °C the total amount of the 6 ML Fe has diffused into the Pd(100) surface but the average concentration is still 46% Fe.

The relative core level binding energy of 0.14 eV comparing the RT grown film to the 400 °C annealed films and the related 46% Fe and 38% Fe concentrations can be explained by different stages of diffusion of the 6 ML Fe room temperature grown and 350 °C annealed film whereas the 400 °C annealing leads to a complete dilution of the iron into Pd(100).

The shift in energy recorded by photoemission can be compared to the Pd *L*_{2,3} absorption edge shifts, measured for RT grown Fe/Pd multilayers.²⁸ The average measured Pd *L*_{2,3} absorption edge leads to shifts of 1 eV for 2 ML Pd spacer up to 0.6 eV for the 8 ML Pd spacer, relative to thick Pd spacers. Assuming that our thin Fe/Pd(100) films are model systems of the multilayered Fe/Pd interfaces, the two previous described MBE multilayers are most probably alloy like.

The LEED patterns observed for the 1–4 ML Fe/Pd(100) films show large 1×1 spots and a large background compared to the clean Pd(100) diffraction. This corresponds

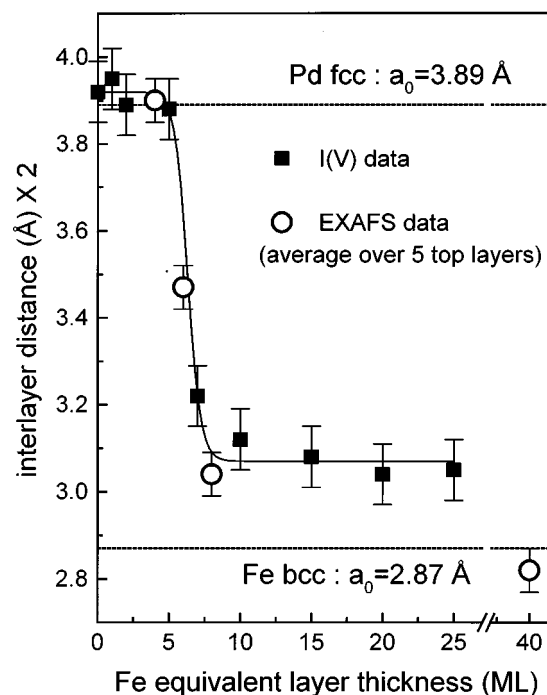


FIG. 3. Evolution of the out of plane parameter with the total equivalent film thickness (ML). The closed squares are the LEED intensity versus voltage $-I(V)$ extracted parameters. The open circles are the parameters determined by EXAFS for the five top layers.

qualitatively to small ordered domain sizes superimposed to disordered areas in the plane of the ultrathin films. Moreover, because of the poor quality of the LEED spots, it was not possible to extract a reliable in-plane parameter evolution during the first stages of the growth. In order to determine modifications of the out of plane parameter we performed $I(V)$ curves obtained on the specular 00 spot in the thickness range of 0 to 25 ML. The extracted out of plane lattice parameters are plotted in Fig. 3 as a function of the equivalent thickness (ML) of iron deposited. The constant lattice parameter of 3.90 Å from 0 to 5 ML leads to the conclusion that there is no evolution of the out of plane distances on the surface of this films. The parameter corresponds to the Pd(100) single crystal spacing and is the first indication for an fcc epitaxial structure of the grown film. Moreover, the rapid transition of the spacing distance after 5 ML, towards the smaller value of 3.1 Å could be explained by a structural transition from a tetragonal distorted fcc to a bcc structure. The strong modification of the out of plane interlayer distances observed on the $I(V)$ curves would thus be coherent with an extended interface alloy or a complete diffusion of the deposited Fe atoms below the LEED detection limit. The absence of chemical information in the $I(V)$ curves leaves open the details of the mixed interface. Considering a five atomic layer average for the $I(V)$ information, the strong reduction of the interlayer distance observed after 5 ML Fe/Pd(100) is coherent with the photoemission data. The two experiments are focused towards the 4–5 ML equivalent thicknesses where simultaneously the chemical and the structural parameters are changing.

For the 10 ML Fe/Pd(100) film the reduced mean free

path of the $I(V)$ technique is not able to discriminate between the uniform bct structure and the superimposed fct and bct structures along the growth direction. Confirmation of the description of the interface grown at room temperature and a more quantitative description of the local chemical and crystallographic structure of the 4 ML film, will be provided by the EXAFS experiment.

Surface extended x-ray absorption fine structure (SEXAFS) has been performed and analyzed for different *in situ* grown ultrathin films. The thicknesses studied here are 4, 6, 8, and 40 ML Fe/Pd(100). The analysis of the EXAFS fine structures and of the Fourier-transformed spectra obtained on the Fe K edge provides a detailed knowledge of the interface structure. This method is element selective because the EXAFS above the K edge of Fe depends exclusively on the Fe local environment. Since it is only sensitive to the local order around an absorbing atom (Fe in our case) we should get a pure fcc signature for the film even if it is composed of differently rotated fcc grains. In this sense SEXAFS is complementary to long range diffraction techniques like LEED or grazing incidence x-ray diffraction. The Fourier transform of the SEXAFS spectrum roughly provides the different shells of neighbors of the absorbing Fe atoms. These relative intensities of these peaks are characteristic of a crystallographic structure: fcc, bcc, hcp.³⁷

The EXAFS signal depends on the angle between the electric field vector ε and the bonding axis \mathbf{r} from absorber to a neighbor^{38–40} through the electric dipole transition operator $\varepsilon \cdot \mathbf{r}$. Thus, we are able to study the structural anisotropy of the film (in-plane versus out of plane bound directions). The structure and the strain can be quantitatively described as a function of the film thickness through the coordination number N and radial distances R of the nearest neighbors (NN). The linear polarization of the synchrotron radiation allows to separate the two contributions (related to in and out of plan bonds) since, for the single-scattering part of the EXAFS signal, the contribution of each bond is weighted by a factor $\cos^2 \alpha$, where α is the angle between the bond and the polarization vector of the x rays. In this framework the effective number of atoms N_i^* of the shell i is given by the sum over all the neighbors j located at the distance R_j :

$$N_i^* = \sum_j 3 \cos^2 \alpha_{ij}, \quad (2)$$

where α_{ij} is the angle between the electric field vector ε and the direction of the atom j of the shell i .

For example, in the case of an fcc (100) structure each atom has 4 NN in the same (100) plane and 8 NN above and below [see Fig. 4(a)]. For a normal incidence of the light (in-plane orientation of the polarization vector ε) the effective coordination numbers are $N_{\text{in}}^* = 6$ and $N_{\text{out}}^* = 6$ where the subscript in and out represent the in-plane and the out-of-plane NN. For a grazing incidence of the light (out of plane orientation of the polarization vector ε) the effective coordination numbers are $N_{\text{in}}^* = 0$ and $N_{\text{out}}^* = 12$. This numbers shows that in the grazing incidence experiment we can measure the R_{out} distance. In normal incidence geometry we will have a mixed contribution of in-plane and out-of-plane bonds.

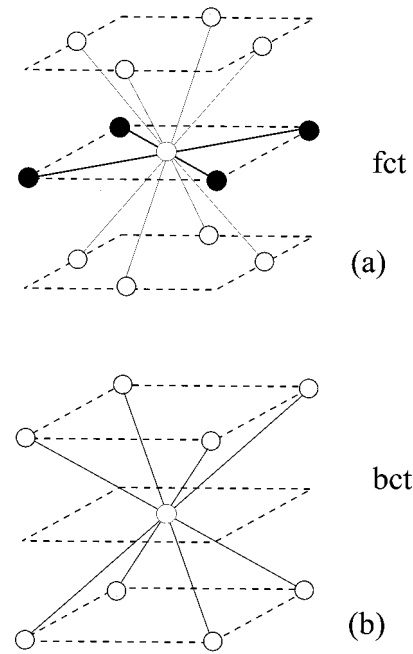


FIG. 4. Schematic representation of the (100) planes in a fct crystal (a) and in a bct crystal (b). Open circle: central emitter atom. Closed circles: “in-plane” first neighbors of the central atom. Gray circles: “out-of-plane” first neighbors of the central atom.

In a bcc (100) structure [see Fig. 4(b)] each atom has 8 first NN (4 in the plane and 2 out-of-plane). In normal incidence the effective coordination numbers are $N_{\text{in}}^* = 8$ (first nearest neighbors) and $N_{\text{2in}}^* = 6$ (second nearest neighbors). In grazing incidence the effective coordination numbers are $N_{\text{1out}}^* = 8$ (first nearest neighbors) and $N_{\text{2out}}^* = 6$ (second nearest neighbors). This shows that the contribution of the first shell of neighbors is identical for the two x-ray incidences. On the contrary, for the second shell of neighbors only the in-plane bonds contribute in normal incidence and only the out-of-plane bonds in grazing incidence.

Figure 5 shows selected EXAFS spectra recorded in the two incidences for 4, 8, and 40 ML. We notice a drastic change in the shape and amplitude of the EXAFS oscillations in the region of 7220–7320 eV for the 4 ML film as compared to the 40 ML film. This evidences a different local environment (structural or chemical) for the absorbing atom. Spectra recorded in normal incidence are different from those recorded in grazing incidence, showing that for all samples the structure is not isotropic. The anisotropy is also clear on the Fourier transform of the spectra shown in Fig. 6. Qualitatively, we observe in the FT spectra two peaks labeled A and B (in the normal and in the grazing incidence geometry) which are present for all our thin films grown at room temperature. This double structure due to Pd environment completely vanishes for 40 ML Fe/Pd(100).

To determine precisely the structure of the films the inverse Fourier transform (IFT) (Fig. 7) of the first peak of the FT has been calculated. These functions are simulated using the classical EXAFS formula to determine the NN distances, the related N^* and the associated Debye Waller factor. The scattering functions (amplitude and phase) are experimentally determined on bulk cobalt for the simulation of Fe-Fe

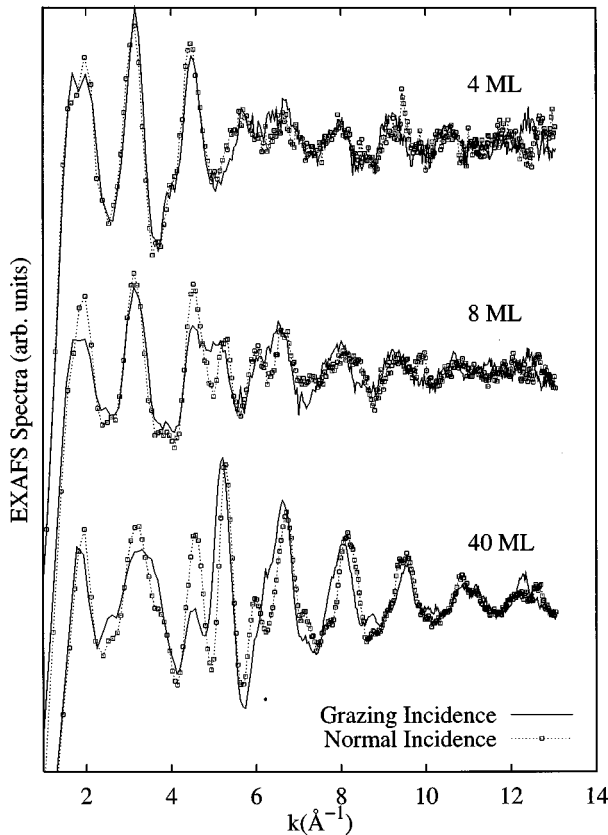


FIG. 5. EXAFS spectra for 4, 8, and 40 ML Fe/Pd(100) grown at room temperature, in normal incidence at 0° (open squares-dotted lines) and in grazing incidence at 75° (continuous lines).

bonds. The scattering parameters for the Fe-Pd neighbors are calculated with the FEFF code.⁴¹ With this set of scattering parameters we simulate the IFT spectra by a coherent fit of the structural parameters (N_i^* , R_i , Debye Waller factor σ_i).

We will first focus on the 4 ML ultrathin film and compare the results to the bcc iron obtained at 40 ML. The results of the best fit obtained on the EXAFS-IFT spectra are summarized in Table I and plotted on Fig. 7. Describing the 4 ML situation, the best fit is obtained with 12 NN (including Fe and Pd neighbors) with $R_i = 2.70 \pm 0.02 \text{ \AA}$ in grazing incidence and $R_i = 2.67 \pm 0.02 \text{ \AA}$ in normal incidence. Assuming a fct (100) structure, in grazing incidence the measured distance is the out-of-plane distance, while in normal incidence the measured distance is the average value between the NN distance in the plane and the NN out-of-plane ($N_{in}^* = 6$ and $N_{out}^* = 6$). This assumption leads to a fct structure with in-plane NN distances of 2.64 \AA and an out-of-plane NN distance of 2.70 \AA . Thus the fct structure has an in-plane lattice parameter $a = 3.73 \pm 0.02 \text{ \AA}$ and a out-of-plane lattice parameter $c = 3.90 \pm 0.02 \text{ \AA}$. The 4 ML Fe/Pd(100) room temperature grown film is thus described by a fct disordered FePd surface alloy. We notice that the in-plane and out-of-plane values R_i (2.64 and 2.70 \AA) are close to 2.69 \AA which is the NN distance of Fe-Pd in a disordered fcc $\text{Fe}_{50}\text{Pd}_{50}$ alloy. The surface alloy can thus be described by a in-plane compressed and out-of-plane extended fct structure [Fig. 4(a)] similar to the tetragonalized γ phase of the disordered $\text{Fe}_x\text{Pd}_{1-x}$ alloy.

From the effective coordination numbers in grazing inci-

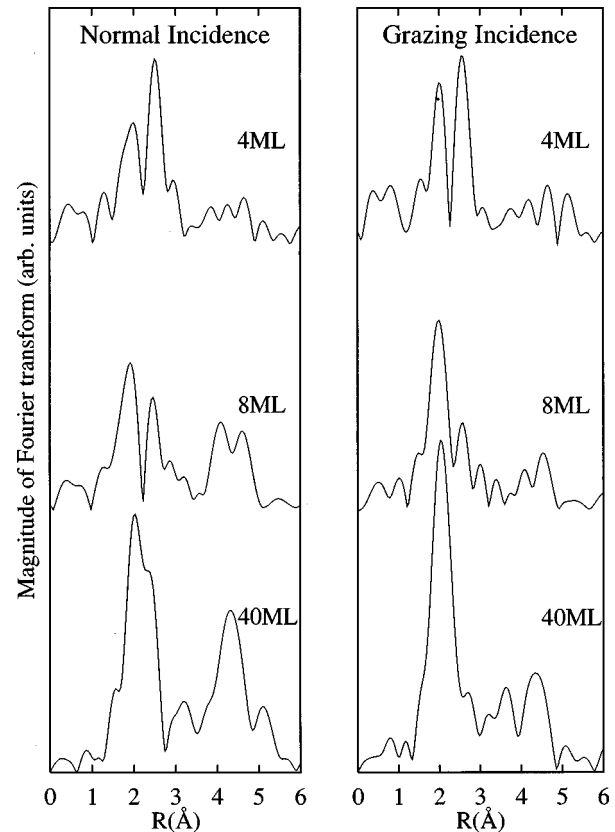


FIG. 6. Fourier transforms (FT) of $k \cdot \chi(k)$ between $k = 2.43 \text{ \AA}^{-1}$ and $k = 12.27 \text{ \AA}^{-1}$ for EXAFS spectra recorded at 300 K in normal incidence and in grazing incidence for 4, 8, and 40 ML Fe/Pd(100).

dence we extract the Fe (respectively, Pd) density of the on top and underneath layer with respect to the iron emitter. Considering the Fe-Fe effective coordination number ($N_{\text{Fe-Fe}}^* = 4.5 \pm 0.5$) or the Fe-Pd effective coordination number ($N_{\text{Fe-Pd}}^* = 7.5 \pm 0.5$) we conclude that the out of plane distribution (perpendicular to the surface) favors the Pd atoms in the local distribution of the Fe emitter. The eight out-of-plane neighbors are constituted of $N_{\text{out Fe-Fe}} = 3.0 \pm 0.5$ and $N_{\text{out Fe-Pd}} = 5.0 \pm 0.5$. Using also the values of the effective number in normal incidence we can deduce that the in-plane neighbors are $N_{\text{in Fe-Fe}} = 2.0 \pm 0.5$ and $N_{\text{in Fe-Pd}} = 2.0 \pm 0.5$. Supporting the numbers N_i involved in the Fe-Fe and Fe-Pd bonds we can propose a local description of the iron environment for 4 ML Fe/Pd(100).

The description of the fct alloy given by the EXAFS analysis shows that the environment of the iron atoms in the plane parallel to the surface is equiatomic whereas the nearest adjacent layers are Pd enriched. The total number of NN of the Fe emitter are $N_{\text{Fe-Fe}} = 5.0 \pm 0.5$ and $N_{\text{Fe-Pd}} = 7.0 \pm 0.5$ Pd.

Considering a disordered alloy, the mean concentration can be calculated by integrating the emitter Fe atom in the total number of 4 atoms in the fct unit cell. This gives per unit cell an overall of 2.2 ± 0.5 Fe atoms and 1.8 ± 0.5 Pd atoms, i.e., a mean concentration of $\text{Fe}_{55}\text{Pd}_{45}$.

For the situation of 4 ML Fe/Pd(100) one can conclude to a fct disordered interface alloy which is tetragonalized and has a nearly equiatomic concentration $\text{Fe}_{55}\text{Pd}_{45}$. This is co-

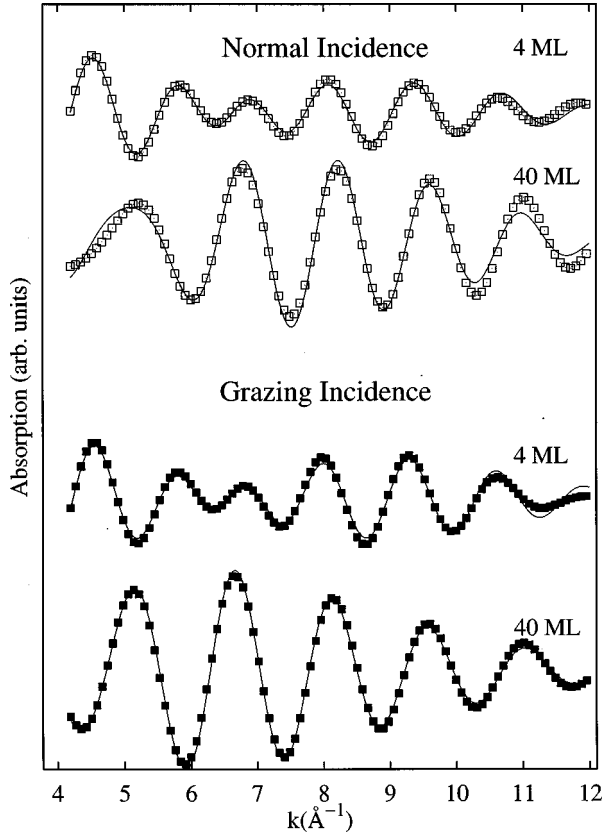


FIG. 7. Simulation of the inverse Fourier transforms of the first shell for 4 and 40 ML Fe/Pd(100) grown at room temperature, in normal incidence at 0° (open squares) and in grazing incidence at 75° (black squares). The experimental data (squares) are superposed to the FEFF simulations (continuous lines).

herent with the photoemission data. It should be pointed out that the average density in the interface region could be less than 55% Fe since EXAFS probes only the local environment of the iron emitter. Considering the total amount of equivalent Fe (4 ML) and the maximum concentration of iron involved in the alloy (55%) almost 8 atomic layers of disordered alloy are needed to describe the interface.

The fct structure with the in-plane lattice parameter $a = 3.73 \pm 0.02 \text{ \AA}$ and out-of plane lattice parameter $c = 3.90 \pm 0.02 \text{ \AA}$ is coherent with the high Pd density in the out of plane direction. Moreover, this situation is favored if thermodynamics is considered because of the very low surface free energy of Pd (2.04 J m^{-2}) with respect to Fe (2.94 J m^{-2}).⁴²

The very bad 1×1 LEED at this stage of the growth is also coherent with a short range order of a (100) surface where the 3% difference between the Pd(100) substrate lattice parameter of 3.89 \AA and the in-plane lattice parameter of $3.775 \pm 0.02 \text{ \AA}$ of the disordered FePd alloy is released by defects and strain, leading to a short range order in the surface alloy.

The thick 40 ML Fe/Pd(100) film is analyzed assuming that the film is homogenous and that the interface alloy can be neglected. This simplification is supported by the FT spectrum at this coverage which shows a first peak with one single structure. For a bcc or bct phase the EXAFS-FT first peak contain the 8 first nearest neighbors and the 6 second nearest neighbors in grazing as well as in normal incidence.

The EXAFS data corresponding to the 40 ML Fe/Pd(100) film can perfectly be simulated by a tetragonalized bct structure of pure iron without any Pd. In Table I we summarize the parameters of the bct structure (in *italic*) which give the best simulation of the EXAFS data. The number of NN are those of a bct structure (8 first neighbors and 6 second neighbors). Moreover, the extracted distance for the first shell of neighbors is the same in both incidences $R_{1\text{Fe-Fe}} = 2.46 \pm 0.03 \text{ \AA}$. For the second shell we measure in normal incidence $R_{2\text{in}} = 2.77 \pm 0.03 \text{ \AA}$ and in grazing incidence $R_{2\text{out}} = 2.82 \pm 0.03 \text{ \AA}$. This leads to the bct tetragonal structure composed of pure Fe with an in-plane lattice parameter $2.77 \pm 0.03 \text{ \AA}$ and an out-of-plane lattice parameter $2.82 \pm 0.03 \text{ \AA}$.

This evidences a partial remanence of the out of plane tetragonalization of the fct alloy in the 40 ML film. In this range of thicknesses the same tetragonalization was observed by a complete analysis of LEED- $I(V)$ curves by Quinn *et al.*²⁷

There are two ways of matching the bct pure iron and the interface fct alloy. The first can be obtained by an abrupt change of the fct structure to the bct one. This could be achieved by a rotation of 45° of the bct lattice in order to match in the plane the fct lattice ($3.73 \pm 0.02 \text{ \AA}$). In this situation the bct Fe lattice of $2.77 \pm 0.02 \text{ \AA}$ (after the EXAFS average value at 40 ML) has to match with the diagonal of the fct lattice which is $2.64 \pm 0.02 \text{ \AA}$. The second possibility for the transition between the alloy and the bct Fe could be an intermediate phase, different from the previously defined fct or bct.

The spectrum for 6 or 8 ML cannot be described by a unique phase (fct or bct). We choose a linear combination of the previously characterized parameters for the fct alloy structure (4 ML Fe/Pd) and for the bct Fe (40 ML Fe/Pd). In

TABLE I. Structural parameters obtained from the fits of the EXAFS signal of the first shell of neighbors for the 4 ML Fe/Pd(100) and 40 ML Fe/Pd(100) films. The bct structural parameters are given in *italic*. The first and second nearest neighbors are indicated for this structure.

| Sample | Type of NN | Normal incidence | | | Grazing incidence | | |
|--------|----------------|------------------------|-----------------------------------|---|------------------------|-----------------------------------|---|
| | | N^* (± 0.5) | $R(\text{\AA})$ (± 0.02) | $\sigma^2(\text{\AA}^2)$ (± 0.001) | N^* (± 0.5) | $R(\text{\AA})$ (± 0.02) | $\sigma^2(\text{\AA}^2)$ (± 0.001) |
| 4 ML | Fe-Fe | 5.2 | 2.67 | 0.014 | 4.5 | 2.70 | 0.004 |
| fct | Fe-Pd | 6.8 | 2.67 | 0.005 | 7.5 | 2.70 | 0.009 |
| 40 ML | <i>Fe-Fe 1</i> | 8.0 | 2.46 | 0.004 | 8.0 | 2.47 | 0.003 |
| bct | <i>Fe-Fe 2</i> | 6.0 | 2.77 | 0.003 | 6.0 | 2.82 | 0.002 |

TABLE II. Structural parameters obtained from the fits of the EXAFS signal of the first shell of neighbors for the intermediate coverages of 6 ML Fe/Pd(100) and 8 ML Fe/Pd(100) films. The bct structural parameters are given in italic. The first and second nearest neighbors are indicated for this structure.

| Sample | Type of NN | Normal incidence | | | Grazing incidence | | |
|--------|----------------|------------------------|-----------------------------------|---|------------------------|-----------------------------------|---|
| | | N^* (± 0.5) | $R(\text{\AA})$ (± 0.02) | $\sigma^2(\text{\AA}^2)$ (± 0.001) | N^* (± 0.5) | $R(\text{\AA})$ (± 0.02) | $\sigma^2(\text{\AA}^2)$ (± 0.001) |
| 6 ML | Fe-Fe | 3.5 | 2.67 | 0.014 | 2.3 | 2.70 | 0.004 |
| | Fe-Pd | 4.5 | 2.67 | 0.005 | 3.7 | 2.70 | 0.009 |
| | <i>Fe-Fe 1</i> | 2.7 | 2.46 | 0.004 | 2.7 | 2.47 | 0.003 |
| | <i>Fe-Fe 2</i> | 1.3 | 2.77 | 0.003 | 2.0 | 2.82 | 0.002 |
| 8 ML | Fe-Fe | 2.6 | 2.67 | 0.014 | 2.3 | 2.70 | 0.004 |
| | Fe-Pd | 3.4 | 2.67 | 0.005 | 3.7 | 2.70 | 0.009 |
| | <i>Fe-Fe 1</i> | 4.0 | 2.46 | 0.004 | 4.0 | 2.47 | 0.003 |
| | <i>Fe-Fe 2</i> | 3.0 | 2.77 | 0.003 | 3.0 | 2.82 | 0.002 |

this case we have adjusted for each thickness (6 and 8 ML) the relative weight between the FePd alloy and the pure Fe bct (in italic in Table II) contributions. The values of R_{in} , R_{out} , N_{Fe}^* and N_{FePd}^* are those of the surface alloy and of the bct structure.

In Table II are shown the results of the best fit for the EXAFS data for 6 and 8 ML films. The 6 ML film is composed of 2/3 alloy and 1/3 bct Fe. For the 8 ML film it is 1/2 alloy and 1/2 bct Fe. We show in Fig. 8 the experimental EXAFS spectra for the 8 ML film and the linear combination of the experimental fct alloy and bct Fe. The coherence between the total equivalent Fe thickness (6 and 8 ML) and the ratio of fct FePd alloy and the Fe bct structure confirm that in both cases the thickness of the FePd alloy is involving 4 ML equivalent Fe and that a pure phase of bct Fe grows on top of the fct alloy.

The out of plane lattice constant given by EXAFS can be corrected for the mean free path and thus be compared to LEED data by averaging the EXAFS lattice constants over the five top layers. Moreover, for the $I(V)$ curve we have to remember the strong influence of the Pd substrate which enhances the first values of the $I(V)$ values. In contrast to this, EXAFS on the Fe K edge gives exclusively the local environment of the Fe atoms.

By averaging the EXAFS out-of-plane parameters over the five top layers the lattice parameters are obtained for 4 ML Fe/Pd(100): $c = 3.90 \pm 0.02 \text{\AA}$; for 6 ML Fe/Pd: $c = 3.47 \text{\AA}$, and for the top of the 8 ML Fe/Pd(100): $c = 3.04 \pm 0.02 \text{\AA}$. The top of the 40 ML film (bct) shows (EXAFS parameters) a lattice constant $c = 2.82 \pm 0.03 \text{\AA}$ close to fcc/Fe one (2.87\AA). These values are all coherent with the $I(V)$ data.

If the EXAFS values and the coherent LEED- $I(V)$ curves (Fig. 2) are compared one observes that the origin of the sudden and strong decrease of the out of plane parameter after 5 ML is related to the structural transition occurring after 4 ML Fe/Pd(100) from a fct disordered alloy toward a bct iron film.

The linear combinations of the EXAFS parameters assuming a reduced mean free path of five atomic equivalent layers supposes that the growth mode of the bct Fe on top of the fct FePd alloy is very smooth. The same condition will be mandatory for the linear combination of the magnetic

properties of the layers for the simulation of the orbital moments that will be presented in the last section. The absence of large bct island growth can be confirmed by Auger As- T curves. The detailed analysis of the different Auger signal evolution and the comparison with low temperature growth kinetics has been published elsewhere.²³ This allows to compare the room temperature growth kinetics with a theoretical layer by layer evolution (exponential decay) for which the mean free path of the substrate Pd 330 eV Auger electrons

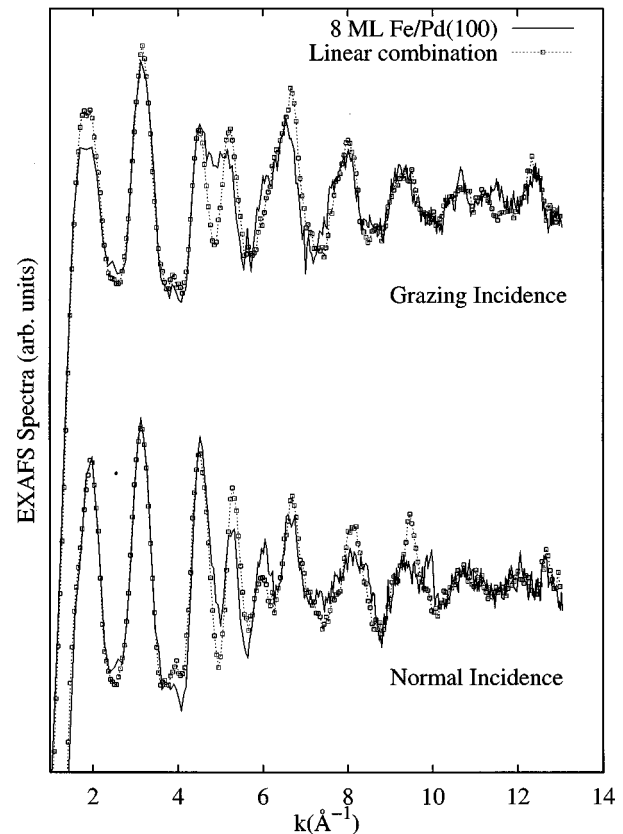


FIG. 8. EXAFS spectra in grazing and normal incidence recorded at 300 K at the iron K edge for 8 ML Fe/Pd(100) (continuous line) compared with the linear combination (open squares-dotted lines) of the experimental EXAFS spectra in the proportion of 1/2 fct alloy (4 ML) and 1/2 bct iron (40 ML).

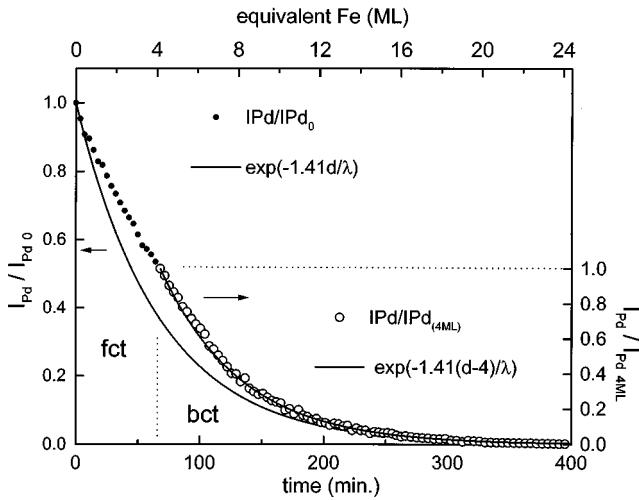


FIG. 9. Auger spectra versus time (AS-T) curve of the Pd_{MNN} (330 eV). Auger transition recorded during the growth of Fe/Pd(100) at room temperature. The growth rate was of 0.2 ML min^{-1} . The closed and open circles are the continuation of the same AS-T curve. The open circles (right scale) represents the AS-T curve for the growth of Fe on the interface formed at 4 ML.

was estimated at 7.2 \AA . In order to simulate the Auger kinetics of the substrate signal at room temperature we suppose that the growth of bct iron begins after 4 ML Fe/Pd(100). Thus we simulate the growth of the fifth, sixth, etc. equivalent Fe layers on top of the previously defined alloy. In Fig. 9 we have renormalized the Pd intensity to 1 at 4 ML (right scale) and superposed to the experimental Auger data the simulated layer by layer growth taking strictly the same parameters (mean free path, flux, layer thickness, etc.) as done for the overall growth. As it can be seen, the experimental points (open circles) stay very close to the layer by layer simulation. This is a confirmation of the nearly layer by layer growth of the bct Fe layers on top of the fct FePd alloy. This justifies the linear combination of the structural and magnetic parameters of the defined FePd alloy and the individual monolayers of bct Fe.

V. DISCUSSION

From the photoemission spectra the interface can be understood as an averaged $\text{Fe}_{50}\text{Pd}_{50}$ alloy up to 4 ML Fe/Pd(100). The SEXAFS data show that locally, the iron atoms are embedded in the Pd(100) surface and that the film can be described as a fct disordered alloy tetragonalized along the [100] direction, normal to the surface plane. The SEXAFS experiment shows that the fct surface alloy is not homogeneous in the local environment of Fe. The equiatomic FePd layers are covered by almost one Pd enriched layer leading to a +4% out-of-plane tetragonalization. This is in agreement with surface free energy considerations.

Let us compare the structure of the Fe/Pd(100) thin films with the MBE grown $\text{Fe}_{50}\text{Pd}_{50}/\text{MgO}$ alloys.³⁰ The diffusion mechanism in FePd, responsible for the microscopic structure of the surface alloy is very similar to the one responsible for the MBE coevaporated $\text{Fe}_{50}\text{Pd}_{50}/\text{MgO}(100)$.^{30,31} The two systems are defined by tetragonalized disordered phases of the $\text{Fe}_{50}\text{Pd}_{50}$ alloy with +4% (surface alloy) and -2 to

TABLE III. Compared ratio of the magnetic moments ratio obtained by MCXD (M_L/M_S) (Ref. 24) and the simulated ratio by linear combination of two reference values taken for the 3 ML Fe/Pd(100) and respectively for the 25 ML Fe/Pd(100) situation representing the fct FePd alloy and respectively the bct thin Fe film growing on this surface alloy. The 40 ML film, compared to the mean free path of the absorption experiment in MCXD ($\lambda=17 \text{ \AA}$) is considered as strongly relaxed compared to the 25 ML film and cannot be considered in our linear combination at the near interface.

| | $M_L/M_S(\text{MCXD} \pm 0.03)$ | M_L/M_S model |
|-------------------|---------------------------------|-----------------|
| Equiv. Fe/Pd (ML) | | |
| 2 | 0.230 | 0.225 |
| 3 | 0.225 ref. fct alloy | 0.225 |
| 5 | 0.200 | 0.200 |
| 10 | 0.160 | 0.150 |
| 25 | 0.100 ref. bct Fe | 0.107 |
| 40 | 0.050 | 0.050 |

-8% (MBE $\text{Fe}_{50}\text{Pd}_{50}$) tetragonalization along the out of plane [100] direction. Nevertheless the observed lattice distortion for the surface alloy is opposite to the one observed in the ‘‘bulk’’ coevaporated alloy. The stabilized phase of our surface alloy ($a=3.73 \text{ \AA}$, $c=3.90 \text{ \AA}$) leads to the ratio $c/a=1.05$ whereas the coevaporated $\text{Fe}_{50}\text{Pd}_{50}$ shows $c/a=0.98$ for the disordered alloy and 0.94 for the ordered $L1_0\text{Fe}_{50}\text{Pd}_{50}$ phase.^{30,31} The main structural difference between the two systems is that the surface alloy is favoring the out of plane extension whereas in bulk systems the compression of the fct lattice is favored. Theoretical calculations which confirm the different stable configurations will be published elsewhere.⁴³

Stabilization of the tetragonalized $\text{Fe}_{50}\text{Pd}_{50}$ surface alloy leads to a new understanding of the different magnetic properties. The in-plane anisotropy (magneto-optical Kerr effect measurements) and the large orbital moment of $0.52\mu_B$ for the 3 ML films [measured on the Fe $L_{2,3}$ edge by MCXD (Ref. 24)] can be directly related to the structure of the tetragonal alloy. This will be supported by comparing the magnetic orbital moments of the Fe/Pd(100) ultrathin films with the MBE grown alloys.

Considering magnetic anisotropy, the fct surface alloy exhibits in-plane anisotropy as observed by Kerr and is coherent with the defined structure (disordered $\text{Fe}_{50}\text{Pd}_{50}$ alloy shows in-plane anisotropy whereas only the perfect ordered $L1_0$ phase shows perpendicular magnetic anisotropy^{30,31}).

Quantitative orbital moments and orbital to spin ratio R measured for the fct surface alloy Fe/Pd(100) and for MBE coevaporated $\text{Fe}_{50}\text{Pd}_{50}$ alloys show similarities. The different tetragonalization (or c/a ratios) in the $\text{Fe}_{50}\text{Pd}_{50}$ alloys³¹ can be thought as proportional and characteristic for the orbital moments: $M_L=0.22\mu_B$ for -2% ($c/a=0.98$) and $M_L=0.42\mu_B$ for -8% ($c/a=0.94$). The orbital moment measured for the 2 ML Fe/Pd(100) surface alloy indeed leads to $M_L=0.52\mu_B \pm 0.06\mu_B$ for a tetragonalization of +4% ($c/a=1.04$). The orbital moments of the different FePd alloys are thus all in agreement with a tetragonalization dependence of the M_L values. Also, for ultrathin films the effect of the reduced dimensionality has to be considered. Surface magnetoelastic contributions could nevertheless enhance the orbital moment as compared to the coevaporated ‘‘bulk’’ alloy.

In this framework, we can explain the dependence of the orbital to spin ratio R with the Fe/Pd(100) film thickness in Ref. 24. The two step model describing the growth at RT (fct Fe₅₅Pd₄₅ alloy up to 4 ML followed by bct Fe layers) can be used to describe the evolution of the orbital magnetic moment. Hole numbers which are known to be sensitive to the chemical environment and to the structure of the magnetic films are involved in the previous determination of the orbital magnetic moments using the MCXD sum rules.²⁴ Thus, we will discuss the experimental values of the ratio $R = M_L/M_S$ as extracted from the published MCXD data.²⁴ If the ratio R is related to the superposition of the two structures (fct and bct) in the Fe/Pd(100) films then it can be interpolated for the intermediate film thicknesses by the linear combination of the value $R = 0.225 \pm 0.03$ measured for the surface alloy at 4 ML Fe/Pd(100) with $R = 0.10 \pm 0.03$ measured for the tetragonalized bct iron at 25 ML Fe/Pd(100). Considering the MCXD related mean free path of $\lambda = 17 \text{ \AA}$ we consider that the ratio R and the magnetic moments of the nearly relaxed 40 ML film are different from the ones measured for the 25 ML film. In Table III, we compare the measured values and the calculated ratio $R = M_L/M_S$ considering two phases (fct alloy and bct Fe) and their values of R corrected for the mean free path of $\lambda = 17 \text{ \AA}$. The very good agreement between the experimental and the linear combination of the previously defined two phases is again a clear indication of the structure related orbital to spin ratio R

in the Fe₅₀Pd₅₀ alloys and explain the decreasing values of R as a function of thickness in our previous work.²⁴

VI. SUMMARY

We described the growth and the interface of Fe/Pd (100) ultrathin films grown at room temperature by core level photoemission, $I(V)$ and EXAFS. The different techniques give a coherent description of the diffusion occurring for the first 4 ML Fe deposit. A structural transition occurs after 4 ML where a fct Fe₅₅Pd₄₅ alloy structure is evidenced with a further deposit of bct pure iron layers. A local description of the diffused interface has been proposed on the basis of the EXAFS parameters. The strong decrease of the lattice parameter observed with the $I(V)$ curves after 4 ML is clearly supported by EXAFS and explained by the structural transition from a fct alloy to bct Fe occurring at 4 ML Fe/Pd(100). At room temperature, the Fe/Pd(100) interface can be described by a disordered Fe₅₅Pd₄₅ alloy with a 4% lattice tetragonalization along the growth direction.

Comparing the magnetic properties obtained by Kerr and MCXD for MBE coevaporated Fe₅₀Pd₅₀ ‘‘bulk’’ alloys and the ultrathin Fe/Pd(100) film leads to the conclusion that the in-plane anisotropy and the large orbital moment measured on the Fe $L_{2,3}$ for the 3 ML Fe/Pd(100) film are directly related to the interface alloying and tetragonalized fct structure.

*Present address: MAX-Lab, Lund, Sweden.

¹F. J. A. den Broeder, D. Kuiper, A. P. van de Mosselaer, and W. Hoving, *Phys. Rev. Lett.* **60**, 2769 (1988).

²W. Reim and P. Wachter, *Phys. Rev. Lett.* **55**, 871 (1985).

³M. Tischer, O. Hjortstam, D. Arvanitis, J. Hunter Dunn, F. May, K. Baberschke, J. Trygg, J. M. Wills, B. Johansson, and O. Eriksson, *Phys. Rev. Lett.* **75**, 1602 (1995).

⁴W. L. O'Brien and M. P. Tonner, *Phys. Rev. B* **49**, 15 370 (1994).

⁵J. Thomassen, F. May, B. Feldmann, M. Wuttig, and H. Ibach, *Phys. Rev. Lett.* **69**, 3831 (1992).

⁶J. Hunter Dunn, D. Arvanitis, and N. Martensson, *Phys. Rev. B* **54**, R11 157 (1996).

⁷J. Shen, R. Skomski, M. Klaua, H. Jenniches, S. Sundar Manoharan, and J. Kirschner, *Phys. Rev. B* **56**, 2340 (1997).

⁸B. Ujfalussy, L. Szunyogh, P. Bruno, and P. Weinberger, *Phys. Rev. B* **77**, 1805 (1996).

⁹D. Weller, J. Stöhr, R. Nakajima, A. Carl, M. G. Samant, C. Chappert, R. Mégy, P. Beauvillain, P. Veillet, and G. A. Held, *Phys. Rev. Lett.* **75**, 3752 (1995).

¹⁰J. Thiele, C. Boeglin, K. Hricovini, and F. Chevrier, *Phys. Rev. B* **53**, R11 934 (1996).

¹¹D. Weller, Y. Wu, J. Stöhr, M. G. Samant, B. D. Hermsmeier, and C. Chappert, *Phys. Rev. B* **49**, 12 888 (1994).

¹²Y. Wu, J. Stöhr, B. D. Hermsmeier, M. G. Samant, and D. Weller, *Phys. Rev. Lett.* **69**, 2307 (1992).

¹³P. Bruno, *Vorlesungsmanuskripte des IFF-Ferienkurs Magnetismus von Festkörpern und Grenzflächen* (forschungszentrum Jülich GmbH, Jülich, 1993), p. 24.1.

¹⁴P. Bruno and J. P. Renard, *Appl. Phys. A: Solids Surf.* **49**, 499 (1989).

¹⁵P. Bruno, *Phys. Rev. B* **39**, 865 (1989).

¹⁶R. Wu, D. Wang, and A. J. Freeman, *Phys. Rev. Lett.* **71**, 3581

(1993); R. Wu and A. J. Freeman, *ibid.* **73**, 1994 (1994).

¹⁷R. Wu, D. Wang, and A. J. Freeman, *J. Magn. Magn. Mater.* **132**, 103 (1994).

¹⁸B. Hillebrands, J. Fassbender, R. Jungblut, G. Güntherodt, D. J. Roberts, and G. A. Gehring, *Phys. Rev. B* **53**, 10 548 (1996).

¹⁹J. Stör and H. König, *Phys. Rev. Lett.* **75**, 3748 (1995).

²⁰H. Dürr and G. Van der Laan, *Phys. Rev. B* **54**, R760 (1996).

²¹I. V. Solov'yev, P. H. Dederichs, and I. Mertig, *Phys. Rev. B* **52**, 13 419 (1995).

²²Z. Celinski, B. Heinrich, J. F. Cochran, W. B. Muir, A. S. Arratt, and J. Kirschner, *Phys. Rev. Lett.* **65**, 1156 (1990).

²³X. Le Cann, C. Boeglin, K. Hricovini, and B. Carrière, *Thin Solid Films* **275**, 95 (1996).

²⁴X. Le Cann, C. Boeglin, B. Carrière, and K. Hricovini, *Phys. Rev. B* **54**, 373 (1996).

²⁵C. Liu and S. D. Bader, *J. Magn. Magn. Mater.* **93**, 307 (1991).

²⁶C. Liu and S. D. Bader, *Phys. Rev. B* **44**, 2205 (1991).

²⁷J. Quinn, Y. S. Li, H. Li, D. Tian, F. Jona, and P. M. Marcus, *Phys. Rev. B* **43**, 3959 (1991).

²⁸J. Vogel, A. Fontaine, V. Cros, F. Petroff, J. P. Kappler, G. Krill, A. Rogalev, and G. Goulon, *Phys. Rev. B* **55**, 3663 (1997).

²⁹J. A. C. Bland, C. Daboo, B. Heinrich, Z. Celinski, and R. D. Bateson, *Phys. Rev. B* **51**, 258 (1995).

³⁰V. Gehanno, A. Marty, B. Gilles, and Y. Samson, *Phys. Rev. B* **55**, 12 552 (1997).

³¹P. Kamp, A. Marty, B. Gilles, R. Hoffmann, S. Marchesini, M. Belakhovsky, C. Boeglin, H. A. Dürr, S. S. Dhesi, G. van der Laan, and A. Rogalev, *Phys. Rev. B* **59**, 1105 (1999).

³²C. T. Chen, Y. U. Idzerda, H. J. Lin, N. V. Smith, G. Meigs, E. Chaban, G. H. Ho, E. Pellegrin, and F. Sette, *Phys. Rev. Lett.* **75**, 152 (1995).

³³B. Johansson and N. Martensson, *Phys. Rev. B* **21**, 4427 (1980);

- N. Martensson and B. Johansson, *Solid State Commun.* **32**, 791 (1979).
- ³⁴A. R. Miedema, P. F. de Châtel, and F. R. de Boer, *Physica B & C* **100B**, 1 (1980).
- ³⁵J. N. Andersen, M. Qvarford, R. Nyholm, S. L. Sorensen, and C. Wigren, *Phys. Rev. Lett.* **67**, 2822 (1991).
- ³⁶R. Nyholm, M. Qvarford, J. N. Andersen, S. L. Sorensen, and C. Wigren, *J. Phys.: Condens. Matter* **4**, 277 (1992).
- ³⁷P. Le Fevre, H. Magnan, and D. Chandèsris, *Surf. Sci.* **352-354**, 923 (1996).
- ³⁸J. Thiele, R. Belkhou, H. Bulou, O. Heckmann, H. Magnan, P. Le Fèvre, D. Chandèsris, and C. Guillot, *Surf. Sci.* **384**, 120 (1997).
- ³⁹O. Heckmann, H. Magnan, P. Le Fevre, D. Chandèsris, and J. J. Rehr, *Surf. Sci.* **312**, 62 (1994).
- ⁴⁰S. K. Kim, Y. M. Koo, V. A. Chernov, and H. Padmore, *Phys. Rev. B* **53**, 11 114 (1996).
- ⁴¹J. J. Rehr, R. C. Alberts, and S. I. Zabinsky, *Phys. Rev. Lett.* **69**, 3397 (1992).
- ⁴²L. Z. Mezey and J. Giber, *Jpn. J. Appl. Phys., Part 1* **21**, 1569 (1982).
- ⁴³I. Galanakis, S. Ostanin, M. Alouani, H. Dreyssé, and J. M. Wills (unpublished).